

- Michaelson, C.-L. Ping, J. M. Kimble, *Arct. Alp. Res.* **28**, 414 (1996).
26. J. D. Hamilton, C. A. Kelly, J. W. M. Rudd, R. H. Hessein, N. T. Roulet, *J. Geophys. Res.* **99D**, 1495 (1994).
27. M. Stuiver and H. Polach, *Radiocarbon* **19**, 355 (1977).
28. Samples were collected directly into glass serum vials from ebullition flux (15). Before analysis, water was added to vials to maintain high internal pressures, the sample was shaken vigorously to get dissolved  $\text{CH}_4$  out of

solution, each sample was transferred to a 6-liter stainless steel container with a syringe, and analytical grade-zero air was added.  $\text{CH}_4$  was separated from each sample and combusted. A subsample of the resulting  $\text{CO}_2$  was analyzed for  $^{13}\text{C}/^{12}\text{C}$  by mass spectrometry, and the remaining  $\text{CO}_2$  was catalytically reduced to graphite (29), and its  $^{14}\text{C}/^{13}\text{C}$  values measured by atomic mass spectrometry at the Lawrence Livermore National Laboratory.

29. S. C. Tyler, *J. Geophys. Res.* **91**, 13232 (1986); D. C.

Lowe, C. A. Brenninkmeijer, S. C. Tyler, E. J. Dlugkencky, *ibid.* **96**, 15455 (1991); J. S. Vogel, *Radiocarbon* **34**, 344 (1992).

30. We thank G. W. Kling, W. S. Reeburgh, M. S. Torn, and M. Wahlen for constructive criticism and the Russian Fund for Fundamental Research, the International Science Foundation, and U.S. Department of Energy for financial support.

10 April 1997; accepted 30 June 1997

## Sizes and Ages of Seamounts Using Remote Sensing: Implications for Intraplate Volcanism

Paul Wessel

Satellite altimetry was used to identify and characterize Pacific intraplate seamounts. The gravimetric amplitudes of seamounts appear to be related to the age difference between the sea floor and seamounts; by inverting this relation, pseudo ages can be obtained for undated seamounts. These pseudo ages imply that excursions in seamount volcanism generally correlate with times of formation of large oceanic plateaus.

The Pacific plate may support more than 50,000 seamounts taller than 1 km, yet ~50% of these undersea volcanoes are uncharted because of sparse bathymetric coverage (1, 2). Even fewer (<1%) have been sampled for radiometric dating (3), making assessment of temporal fluctuations in intraplate volcanism uncertain. Because electromagnetic sensing devices cannot penetrate the oceans, we are unable to image the sea floor remotely and instead must rely on surface ships equipped with sonar. At the present rate of data acquisition, complete bathymetric coverage may take centuries. However, the density contrast between seawater and the sea floor basalt gives rise to gravity anomalies. These minute variations in Earth's gravitational pull cause seawater

to be attracted to seamounts, leading to a sea surface (which approximates the geoid) whose shape reflects these underlying fea-

tures (4). Thus, since the early 1980s, satellite altimetry has provided broad coverage of the sea surface or geoid undulations (5). Early attempts to map the seamount distribution were largely limited by the coarseness of the satellite coverage [the typical track spacing was >100 km (6)], and many seamounts went undetected. Because seamounts are typically much smaller than 100 km, it was difficult to estimate what part of the seamount had been traversed by the satellite, leading to large uncertainties in estimates of seamount height and diameter (7).

Recently, the U.S. Navy declassified its Geosat satellite altimetry, which has been combined with the European Space Agency

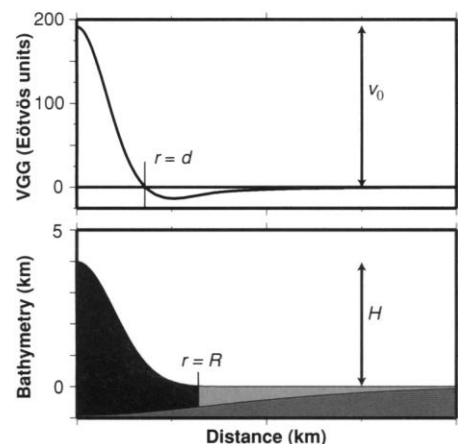


**Fig. 1.** Theoretical VGG over an isostatically compensated seamount of radius  $R$  and height  $H$  (14). The amplitude  $v_0$  and zero-crossing distance  $d$  are the two clearest characteristics of the anomaly.

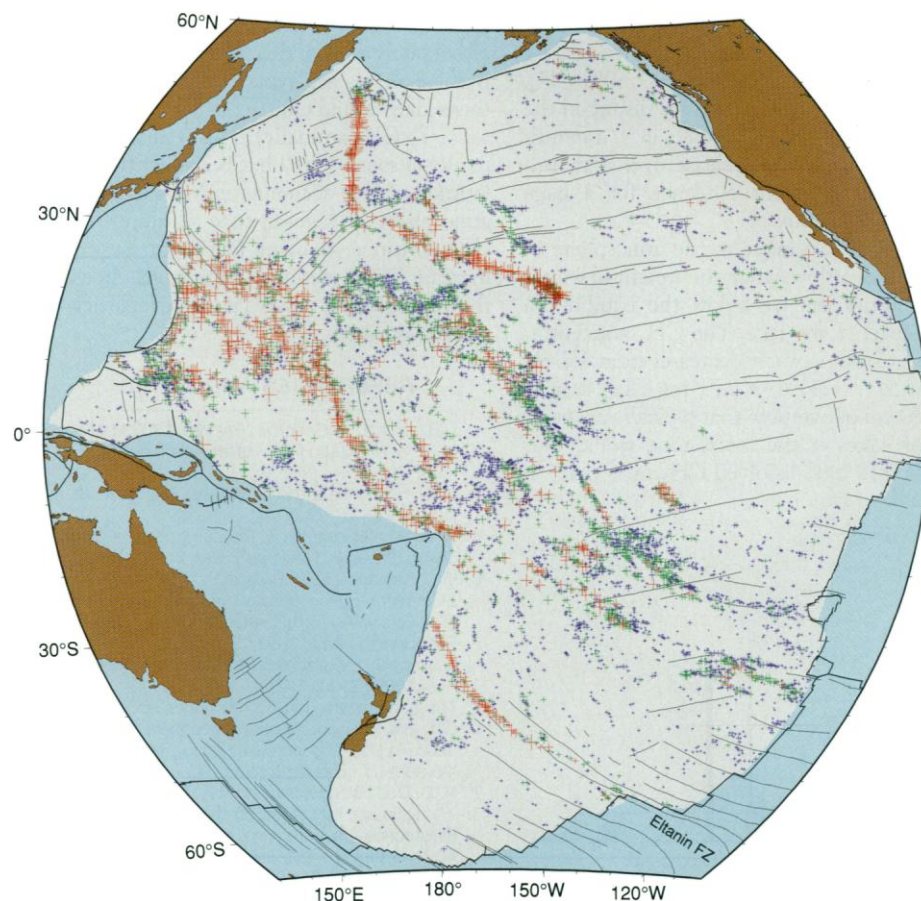


**Fig. 2.** Equal-area Hammer projection showing all 8882 seamounts found on the Pacific plate; the sizes of crosses reflect the VGG amplitudes. Blue crosses are small seamounts (30 to 60 Eötvös units, generally <2.5 km tall), red crosses are large seamounts (>120 Eötvös units, generally >3.5 km tall), and green crosses are of intermediate size. The Eltanin fracture zone is indicated.

ERS-1 altimetry to provide a detailed ( $\sim 10$  km resolution) view of all ocean basins (8). Traditionally, statistical studies of seamount distributions have focused on assessing the spatial variability of volcanism (9). However, most seamounts have not been dated, even though the temporal aspect of intraplate volcanism is the most important to understand. Given the cost (in time and money) of sample acquisition, it is doubtful that we will ever obtain an extensive database of radiometric ages; hence, it is imperative to explore alternatives to the radiometric dating of seamounts.

On the basis of the known sizes and ages of 59 seamounts, a vague but tantalizing relation emerged: Seamount size apparently increased with the square root of the age contrast between the seamount and sea floor [that is, the sea floor age at the time of seamount formation (10)]. This trend could be related to the simple and systematic effects of sea floor maturation (11). Here, I document the existence of such a relation, using a fully automated characterization of seamount shapes on the entire Pacific plate from satellite altimetry to yield pseudo ages for uncharted and unsurveyed seamounts, and I assess the temporal aspects of intraplate volcanism on a large scale.

Rather than using the gridded gravity anomalies (8), my starting point was the gridded vertical gravity gradient (VGG, in Eötvös units), also known as the curvature of the geoid or sea surface (12). Use of the VGG provides for reduced sensitivity to the elastic thickness of the lithosphere and the density of sediments, as well as better spatial separation of overlapping seamounts (13). I preprocessed the VGG grids by removing the longer length scales (using robust median filters) and determined local maxima in the residual data; these are the potential sites of seamounts. Theoretical modeling indicates that VGG anomalies over a Gaussian seamount should have a pronounced zero-crossing somewhat inside the actual seamount radius (14) (Fig. 1). However, because of random noise in the data, the zero-contour meanders and rarely encloses a seamount. I therefore determined the 25-Eötvös unit contour instead and used it to evaluate the potential maxima that fell inside this contour (15). When two or more maxima were contained by the same closed contour, I estimated the individual zero-crossings by evaluating the "volume" under the VGG surface within the contour and distributing this volume among the contained volcanoes, assuming that all the volcanoes inside the contour have the

same height/radius aspect ratio (16). Finally, I excluded all features within 25 km of a known fracture zone or trough, leaving a total of 8882 seamounts on the Pacific plate (Fig. 2). The spatial distribution of small, intermediate, and large seamounts generally confirms earlier results obtained with lower resolution data (17), but adds more higher order details.

Given the dense coverage available, I also estimated the actual bathymetric size of each seamount. For example, the observed VGG (Fig. 3A) can be processed to isolate the seamount signatures only (Fig. 3B) by examining a  $10^\circ$  by  $10^\circ$  area in the central Pacific. By means of forward modeling of seamount VGG of all sizes allowed, I created a numerical look-up table that relates the observed VGG amplitude and zero-crossing distance to actual seamount radius and height (18). Although gravimetric estimates closely correspond to the VGG residual maxima, the bathymetric predictions exhibit uncertainties up to 25% (19) (Fig. 3C). A comparison with available bathymetry (Fig. 3D) shows that in general, the poor bathymetric coverage gives overly smooth bathymetry that in many cases overestimates the size of individual sea-

mounts, and many features are missing entirely (20). Although the predicted sizes of individual seamounts may have significant errors, the robust gravimetric estimates are more than adequate for a variety of purposes, including but not limited to studies of spatial seamount distributions (9), absolute-motion plate tectonic reconstructions (21), hot spot flux estimates (22), stress and elastic thickness (23), and determination of hot spot locations (24).

Of the 8882 seamounts detected, 6306 are located on sea floor of known age (25). A plot of all VGG estimates versus crustal age gives a scatterplot with an upper envelope (Fig. 4). This envelope implies that there is a simple relation between VGG and  $\Delta t$ . The envelope occurs because the VGG over seamounts sitting on sea floor of a given age should be less than or equal to the VGG of the youngest seamount on sea floor of that age; older seamounts will have progressively smaller VGGs because they formed when the sea floor was younger and less able to support a large volcano. This model assumes that all volcanoes grow to their limiting size. The VGG amplitudes for all seamounts of known age contrast (Fig. 4, circles) (3)

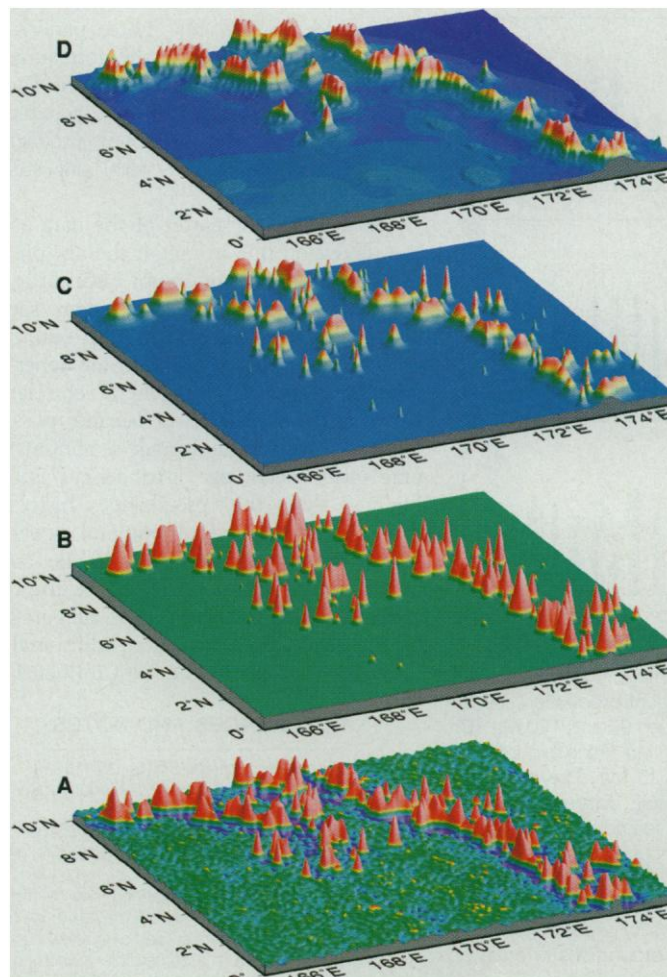


**Fig. 3.** Comparison between observed VGG (A) and VGG shapes of seamounts isolated by my technique (B) for a segment of the Marshall-Gilbert-Ellice chain. The zero-crossing distances and VGG amplitudes were then used with the look-up table to predict seamount radius and heights (C). For comparison, the ETOPO5 bathymetry is shown (D). The regional depth variations evident in the ETOPO5 data have been filtered out in the other images.

Department of Geology and Geophysics, School of Ocean and Earth Science and Technology, University of Hawaii, 1680 East-West Road, Honolulu, HI 96822, USA. E-mail: wessel@soest.hawaii.edu

generally agree with the simple envelope relation. The regression fit to the envelope may thus be inverted to give predictions of sea-

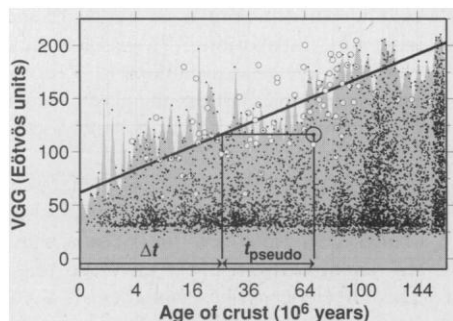


**Fig. 4.** The envelope of maximum values in the scatterplot of seamount VGG versus crustal age reflects a simple square-root relation between seamount size and  $\Delta t$ , which can be inverted to give predictions of pseudo age. For example, the observed VGG value inside the large circle (116.6 Eötvös units) was measured over a seamount on crust 69 million years old. Inversion gives  $\Delta t = 25.6$  million years, implying a seamount (pseudo) age of 43.4 Ma. VGG amplitudes for all seamounts of known age contrast are shown as small circles.

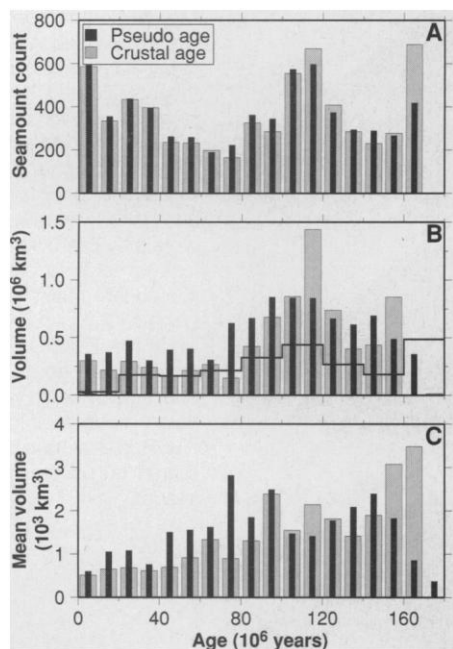


**Fig. 5.** (A) Number of seamounts versus pseudo age or crustal age. Seamount production seems to have been higher between 90 and 120 Ma. (B) Total seamount volumes, indicating higher volumes between 80 and 120 Ma. The solid line represents comparable results obtained from bathymetry (29). (C) Average seamount volume (total volume divided by seamount count), showing peaks during the intervals 70 to 80 Ma, 90 to 100 Ma, and 140 to 150 Ma. Unlike histograms versus crustal ages, the histograms for pseudo ages cannot be normalized by the proportions of crust of different ages.

mount age given VGG and sea floor age (26).

The prediction of an individual seamount's age involves large uncertainties. For example, the horizontal distances from each circle to the regression line (Fig. 4) represent the misfit between known radiometric ages and the corresponding pseudo ages. However, when the large data set is averaged into age categories, the uncertainties decrease substantially. The age predictions are completely decoupled from the bathymetric predictions.

Using the bathymetric predictions and isostatic modeling, I estimated the total seamount volume (extrusive plus moat infill) for all 8882 seamounts (27) (Fig. 5). The data reveal that younger seamounts representing a large cumulative volume sit on mid-Cretaceous [110 to 120 million years ago (Ma)] crust, as evidenced by the shift toward lower age ranges between pseudo ages and crustal ages. Seamounts on the oldest crust actually have pseudo ages that are much younger (Fig. 5). The satellite-derived volumes are almost twice as large as volumes estimated from the available ship bathymetry data sets (28, 29). In view of seamount volumes for both crustal and pseudo ages, larger-than-average seamounts appear to have formed during the intervals 70 to 80 Ma, 90 to 100 Ma, and perhaps 140 to 150 Ma. These periods are generally associated with the formation of several large igneous provinces in the Pacific Ocean (30), although it is not possible to discern whether the seamount production predates, was synchronous with, or postdates plateau formation.

Because of the scatter of the data about the regression line in Fig. 4, the age predictions are neither unique nor necessarily accurate. If factors such as local magma supply or regional stress variations affect seamount size, then our pseudo ages become upper age bounds. However, the general correlation between the formation of oceanic plateaus and the peaks in the average seamount volume versus pseudo-age distribution (Fig. 5C) implies that the pseudo-age histogram should reflect the actual temporal aspects of Pacific intraplate volcanism. While radiometric dating will continue to be the only accurate dating method, pseudo ages are useful in identifying areas where additional radiometric dates would be most influential.

## REFERENCES AND NOTES

1. D. K. Smith, *Rev. Aquatic Sci.* **5**, 197 (1991).
2. C. H. Craig and D. T. Sandwell, *J. Geophys. Res.* **93**, 10408 (1988).
3. B. H. Keating, *Summary of Radiometric Ages from the Pacific* (IOC Tech. Ser. 32, UNESCO, Paris, 1987), pp. 1-67.
4. Sea surface (or geoid) undulations over seamounts are small. A seamount 4 km tall may give rise to an anomaly of a few meters spread over a few hundred kilometers, making it imperceptible to human observers but easily detectable by satellite altimetry.

5. W. F. Haxby, G. D. Kamer, J. L. LaBrecque, J. K. Weissel, *Eos* **64**, 995 (1983); D. T. Sandwell, *J. Geophys. Res.* **89**, 1089 (1984).
6. N. M. Baudry, M. Diament, Y. Albouy, *Geophys. J. R. Astron. Soc.* **89**, 869 (1987); A. R. Lazarewicz and D. C. Schwank, *Geophys. Res. Lett.* **9**, 385 (1982); K. Lambeck and R. Coleman, *ibid.*, p. 389.
7. A. B. Watts and N. M. Ribe, *J. Geophys. Res.* **89**, 11152 (1984).
8. D. T. Sandwell and W. H. F. Smith, *ibid.* **102**, 10039 (1997).
9. D. Chapel and C. Small, *Eos* **77**, F770 (1996); see also (2).
10. D. Epp, *J. Geophys. Res.* **89**, 9991 (1984).
11. As lithosphere ages, it cools and thickens, and is thus able to support larger seamounts. However, a variety of physical models have been proposed, including hydrostatic balance of magma pressure [for example, J. P. Eaton and K. J. Murata, *Science* **132**, 925 (1960); P. R. Vogt, *Earth Planet. Sci. Lett.* **23**, 337 (1974)] and control on size exerted by flexural stresses in the upper lithosphere (23) or volcano flanks [P. J. McGovern and S. C. Solomon, *J. Geophys. Res.* **98**, 23553 (1993)]. These mechanisms all produce a general size-age relation, making it difficult to uniquely identify the primary mechanism [L. Wilson, J. W. Head, E. A. Parfitt, *Geophys. Res. Lett.* **19**, 1395 (1992)].
12. P. Vaníček and E. Krakiwsky, *Geodesy: The Concepts* (North-Holland, New York, 1982). The gravity anomalies (8) are derived from a VGG grid through a Fourier transform; the VGG was obtained by algebraic manipulation of observations and does not contain spectral edge effects. One Eötvös unit is equal to 0.1 mGal km<sup>-1</sup>.
13. Large seamounts depress the crust, reaching an isostatic equilibrium. The shape of such flexural deformation depends on the elastic thickness of the lithosphere and the density of the sediment in the moats [A. B. Watts, *J. Geophys. Res.* **83**, 5989 (1978)]. Because the VGG strongly attenuates long-wavelength signals, the gravitational effect of flexural subsidence beneath a seamount is largely eliminated, making the attraction of the seamount itself the dominant component of the VGG anomaly.
14. Following the method of Craig and Sandwell (2), I approximated all seamounts by Gaussian shapes. The radial VGG signal over such features can be approximated by
 
$$\text{VGG} = \frac{v_0}{2} \left\{ 1 - \left( \frac{r}{d} \right)^2 + \exp \left[ -\frac{9}{2} \left( \frac{r}{d} \right)^2 \right] \right\} \quad (1)$$
 where  $v_0$  is the maximum VGG amplitude,  $r$  is distance from the center, and  $d$  is the zero-crossing distance where  $\text{VGG}(d) = 0$ . Because VGG has a steep slope at  $r = d$ , it is much easier to detect the zero-crossing than comparable features in the geoid free-air anomaly or deflection of the vertical) ( $f$ , 6).
15. I accounted for this adjustment by using the same contour in model calculations.
16. With height proportional to radius, the volume of a single seamount is proportional to  $v_0^3$ . Equating the sum of these volumes to the numerically integrated volume inside the contour allows estimation of individual radii.
17. I found numerous linear seamount chains indicative of hot-spot volcanism and a much higher density of seamounts in the central and western Pacific; the latter also has most of the largest seamounts detected. The lowest seamount densities are found south of the Eltanin fracture zone and in the equatorial eastern Pacific.
18. I used forward modeling of plate flexure caused by Gaussian seamounts of all sizes, low-pass filtered the results to make them spectrally similar to the observed data, and estimated zero-crossings and maximum amplitudes using the same procedures as were applied to the data. The results were compiled into a two-dimensional look-up table that relates maximum VGG and  $d$  to seamount height and flank slope, which combine to yield radius.
19. The observed and predicted volumes appear to agree to within 10 to 15%, but the requirement of a Gaussian shape leads to larger errors in the sea-

mount height and radius estimates.

20. The marine portions of the ETOPO5 data set derive from SYNAPS [R. J. Van Wyckhouse, *Tech. Rep. TR-233* (U.S. Naval Oceanographic Office, NOO-Washington, DC, 1973)] and contain numerous artifacts caused by the combination of poor data coverage, gridding of contours instead of depth soundings, and inappropriate gridding methodology [W. H. F. Smith, *J. Geophys. Res.* **98**, 9591 (1993)].

21. R. A. Duncan and D. A. Clague, in *The Ocean Basins and Margins*, A. E. M. Nairn, F. G. Stehli, S. Uyeda, Eds. (Plenum, New York, 1985), pp. 89–121; R. D. Jarrard and D. A. Clague, *Rev. Geophys.* **15**, 57 (1977); C. Y. Yan and L. W. Kroenke, *Proc. ODP Sci. Results* **130**, 697 (1993).

22. J. P. Morgan, W. J. Morgan, E. Price, *J. Geophys. Res.* **100**, 8045 (1995).

23. U. S. ten Brink, *Geology* **19**, 397 (1991).

24. P. Wessel and L. W. Kroenke, *Nature* **387**, 365 (1997).

25. R. D. Müller, W. R. Roest, J. Y. Royer, L. M. Gahagan, J. G. Sclater, *J. Geophys. Res.* **102**, 3211 (1997).

26. Robust regression of the envelope in Fig. 3 gives  $VGG(\Delta t) = 61.8 + 10.8\sqrt{\Delta t}$ . This is inverted to yield

the empirical relation

$$\text{pseudo age} = \text{seafloor age} - \left[ \frac{VGG(\Delta t) - 61.8}{10.8} \right]^2 \quad (2)$$

27. The flexural modeling also allowed numerical estimation of moat volumes.

28. R. Batiza, *Earth Planet. Sci. Lett.* **60**, 195 (1982).

29. W. H. F. Smith, thesis, Columbia University (1990).

30. The Ontong Java plateau was emplaced during two distinct episodes at ~121 Ma and ~89 Ma [D. Bercovic and J. Mahoney, *Science* **266**, 1367 (1994)]; the Manahiki plateau also formed at ~123 Ma, whereas the Hess rise (90 to 100 Ma) and the Mid-Pacific Mountains (75 to 130 Ma) have longer ranges or ages. The oldest plateau is Shatsky rise (138 to 145 Ma) [R. Larson and P. Olson, *Earth Planet. Sci. Lett.* **107**, 437 (1991)].

31. I thank W. Smith for providing the VGG grid. Supported by NSF grant EAR-9303402. School of Ocean and Earth Science and Technology, University of Hawaii, contribution no. 4517.

17 April 1997; accepted 13 June 1997

## Identification of the Tuberous Sclerosis Gene TSC1 on Chromosome 9q34

Marjon van Slegtenhorst, Ronald de Hoogt, Caroline Hermans, Mark Nellist, Bart Janssen, Senno Verhoef, Dick Lindhout, Ans van den Ouweland, Dicky Halley • Janet Young, Mariwyn Burley, Steve Jeremiah, Karen Woodward, Joseph Nahmias, Margaret Fox, Rosemary Ekong, John Osborne, Jonathan Wolfe, Sue Povey • Russell G. Snell, Jeremy P. Cheadle, Alistair C. Jones, Maria Tachataki, David Ravine, Julian R. Sampson • Mary Pat Reeve, Paul Richardson, Friederike Wilmer, Cheryl Munro, Trevor L. Hawkins • Tiina Sepp, Johari B. M. Ali, Susannah Ward, Andrew J. Green, John R. W. Yates • Jolanta Kwiatkowska, Elizabeth P. Henske, M. Priscilla Short, Jonathan H. Haines, Sergiusz Jozwiak, David J. Kwiatkowski\*

Tuberous sclerosis complex (TSC) is an autosomal dominant disorder characterized by the widespread development of distinctive tumors termed hamartomas. TSC-determining loci have been mapped to chromosomes 9q34 (*TSC1*) and 16p13 (*TSC2*). The *TSC1* gene was identified from a 900-kilobase region containing at least 30 genes. The 8.6-kilobase *TSC1* transcript is widely expressed and encodes a protein of 130 kilodaltons (hamartin) that has homology to a putative yeast protein of unknown function. Thirty-two distinct mutations were identified in *TSC1*, 30 of which were truncating, and a single mutation (2105delAAAG) was seen in six apparently unrelated patients. In one of these six, a somatic mutation in the wild-type allele was found in a TSC-associated renal carcinoma, which suggests that hamartin acts as a tumor suppressor.

TSC is a systemic disorder in which hamartomas occur in multiple organ systems, particularly the brain, skin, heart, lungs, and kidneys (1; 2). In addition to its distinct clinical presentation, two features serve to distinguish TSC from other familial tumor syndromes. First, the tumors that occur in TSC are very rare in the general population, such that several TSC lesions are, by them-

selves, diagnostic of TSC. Second, TSC hamartomas rarely progress to malignancy. Only renal cell carcinoma occurs at increased frequency in TSC (~2.5%) and with earlier age of onset; it appears to arise in TSC renal hamartomas, termed angiomyolipomas (3). Nonetheless, TSC can be a devastating condition, as the cortical tubers (brain hamartomas) frequently cause epilep-

sy, mental retardation, autism, or attention deficit-hyperactive disorder, or a combination of these conditions (1, 4).

TSC affects about 1 in 6000 individuals, and ~65% of cases are sporadic (5). Linkage of TSC to chromosome 9q34 was first reported in 1987, and this locus was denoted *TSC1* (6). Later studies provided strong evidence for locus heterogeneity (7) and led to the identification of chromosome 16p13 as the site of a second TSC locus (denoted *TSC2*) (8). The *TSC2* gene was identified by positional cloning, and the encoded protein, denoted tuberlin, contains a domain near the COOH-terminus with homology to a guanosine triphosphatase (GTPase) activating protein (GAP) for rap1, a Ras-related GTPase (9).

The focal nature of TSC-associated hamartomas has suggested that *TSC1* and *TSC2* may function as tumor suppressor genes. The occurrence of inactivating germline mutations of *TSC2* in patients with tuberous sclerosis (9–11) and of loss of heterozygosity (LOH) at the *TSC2* locus in about 50% of TSC-associated hamartomas (12–14) supports a tumor suppressor function for *TSC2*. In contrast, LOH at the *TSC1* locus has been detected in <10% of TSC-associated hamartomas (13, 14), suggesting the possibility of an alternative pathogenic mechanism for lesion development in patients with *TSC1* disease.

As part of a comprehensive strategy to identify *TSC1*, we identified 11 microsatellite markers from the 1.4-Mb *TSC1* region and developed an overlapping contig (with only a single gap of 20 kb) of cosmid, P1

### The *TSC1* Consortium:

M. van Slegtenhorst, R. de Hoogt, C. Hermans, M. Nellist, B. Janssen, S. Verhoef, D. Lindhout, A. van den Ouweland, D. Halley, Department of Clinical Genetics, Erasmus University and University Hospital, Rotterdam, Netherlands.

J. Young, M. Burley, S. Jeremiah, K. Woodward, J. Nahmias, M. Fox, R. Ekong, J. Wolfe, S. Povey, MRC Human Biochemical Genetics Unit and Galton Laboratory, University College of London, London NW1 2HE, UK.

J. Osborne, University of Bath, Bath BA2 7AY, UK.

R. G. Snell, J. P. Cheadle, A. C. Jones, M. Tachataki, D. Ravine, J. R. Sampson, Institute of Medical Genetics, University of Wales College of Medicine, Cardiff CF4 4XN, Wales, UK.

M. P. Reeve, P. Richardson, F. Wilmer, C. Munro, T. L. Hawkins, Whitehead Institute, MIT Center for Genome Research, Cambridge, MA 02139, USA.

T. Sepp, J. B. M. Ali, S. Ward, A. J. Green, J. R. W. Yates, Departments of Pathology and Medical Genetics, University of Cambridge, Addenbrooke's NHS Trust, Cambridge CB2 2QQ, UK.

M. P. Short, Department of Child Neurology, University of Chicago School of Medicine, Chicago, IL 60637, USA.

J. H. Haines, Molecular Neurogenetics Unit, Massachusetts General Hospital, 149 13th Street, Boston, MA 02129, USA.

S. Jozwiak, Division of Child Neurology, Children's Health Center, 04-736 Warsaw, Poland.

J. Kwiatkowska, E. P. Henske, D. J. Kwiatkowski, Division of Experimental Medicine and Medical Oncology, Brigham and Women's Hospital, Boston, MA 02115, USA.

\*To whom correspondence should be addressed. E-mail: kwiatkowski@calvin.bwh.harvard.edu